Generating Fuzzy Membership Functions for Modeling Wetland Ecosystems From Multispectral Remote Sensing Images

Jifa Guo ⓘ and Shihong Du ⓘ

Abstract—The inherent fuzziness of wetland ecosystems largely accounts for the spectral variability of wetland ecosystems in remote sensing images. In addition, a limited spatial resolution leads to the presence of many mixed pixels in middle-resolution multispectral remote sensing images. The existing methods that use a single center or a limited number of endmembers to represent land cover types cannot fully account for the spectral variability of land cover types; moreover, these methods use these limited representations to calculate the membership function (MF), leading to limited classification and mapping performance. To address spectral variability and mixed pixels, this study proposes a novel MF generation method, in which mixed pixels are treated as an auxiliary type, and the clustering and spectral characteristics are integrated to detect the cores of land cover types in spectral space. Then, the spectral diversity can be fully expressed by the core components of the land cover types. The membership values of mixed pixels are calculated from the core components via the sparse reconstruction method. The experiment shows that the proposed method has a substantial increase in classification accuracy over the existing methods.

Index Terms—Fuzziness, fuzzy set, membership function (MF) generation, spectral variability.

ABBREVIATIONS

MF	Membership function.
FCM	Fuzzy C-means clustering method.
FKNN	Fuzzy k-nearest neighbors method.
FSSC	Fuzzy semisupervised clustering method.
IT2FCM	Interval type-2 FCM clustering method.
NDVI	Normalized difference vegetation index.
MNDWI	Modified normalized difference water index.
$C+1$ FMG	$C+1$ fuzzy membership generation method.
UG	Unlabeled granule.
PG	Pure granule.
SG	Sparse granule.
IG	Impure granule.
BG	Boundary granule.
CG	Core granule.
IGC	Internal granule of core.
FGC	Fringe granule of core.
NPG	New pure granule.
IS_k	k-influence space.
NN	Natural neighbor.
RNN	Reverse nearest neighbor.
NaNE	Natural neighbor eigenvalue.
LPP	Locality preserving projections.
SAM	Spectral angle metric.
SID	Spectral information divergence.
SAM-SID	SAM-SID mixed measure.
JM-SAM	Jeffries–Matusita-spectral angle mapper.
CFDT	C-fuzzy decision tree.
SIIT2-FCM	Semisupervised interval type-2 FCM using spatial information.
SS-AIT2FCM	Semisupervised adaptive interval type-2 fuzzy C-means algorithm.
OA	Overall accuracy.
Fractional SU	Fractional-based sparse unmixing method.

I. INTRODUCTION

WETLANDS are multifunctional and biodiverse ecosystems on Earth and play key roles in food production, water purification and control, air purification, climate regulation, nutrient cycling, flood reduction, and biodiversity conservation [1], [2]; however, they also exhibit intrinsic fuzziness. That is, some locations may partially belong to some wetland components, and there is no clear boundary line between them. For instance, the boundary of a lake often involves a gradual transition zone from shrubs to aquatic plants and then to shallow water, which means that it is difficult to draw a crisp line between water and nonwater areas. For several decades, remote sensing technologies have been widely used for monitoring, managing, and analyzing wetland environments [3], [4], [5], [6], and some studies have focused on the intrinsic fuzziness [7], [8] of wetlands, especially the spectral variability [9] of wetland components. Two types of spectral variability are commonly considered: variability within one class (within-class variability) and similarity among endmember spectra of different classes (interclass variability) [10]. Middle-resolution multispectral remote sensing images, i.e., Sentinel-2 and Landsat 8 images,

are more suitable for mapping wetlands than very high resolution remote sensing images because of their appropriate spatial resolution and low cost. However, due to their limited spatial resolution, mixed pixels are mixtures of different pure materials in these types of images [9]. The presence of spectral variability and mixed pixels has been recognized as two major problems in the remote sensing community. From the wetland classification point of view, some wetland components may be less than the spatial resolution of the middle-resolution image, and the interlaced distribution of small patches will subsequently form many mixed pixels in middle-resolution images. This approach makes boundaries between different land cover types fuzzier. In addition, preprocessing methods, such as geometric correction and image fusion, may introduce uncertainties into remote sensing images, and these methods may also cause blurring of middle-resolution remote sensing images. These phenomena lead to difficulty in wetland classification.

Fuzzy sets provide a more appropriate way to map and analyze the fuzziness of wetlands than traditional Boolean methods [8], [11]. MFs, which express the probabilities of elements partially belonging to fuzzy sets, are used to describe the fuzzy boundaries of wetland components [7] and are the basis of wetland fuzzy classification. Fuzzy clustering and classification methods, such as FCM clustering [12], [13], FKNN [14], fuzzy semisupervised clustering [15], and interval type-2 FCM clustering [16], are often used to classify remote sensing images. MFs should be generated first in these methods, and then the remote sensing images are classified according to the maximum membership principle. In addition, MFs can be used for image processing and understanding [17], land cover classification and subpixel land cover mapping [18], [19], [20], fuzzy geographic object modeling and analysis [21], [22], [23], etc. However, due to the spectral variability and large mixed pixels in middle-resolution remote sensing images, land cover types may have multiple clusters in spectral space, and these clusters may have different shapes and sizes. In addition, mixed pixels also form clusters of different shapes and sizes, and in our experiments, the clusters of mixed pixels may sometimes be larger than those of pure pixel clusters. Since pure pixels are clustered as regions in spectral space and because spectrum mixed pixels may be a combination of spectra of pure pixels of different land cover types of any proportion, the mixed pixels may be located in clusters of land cover types. To our knowledge, this phenomenon has often been ignored in the existing studies. Thus, using clustering characteristics to determine pure pixels may lead to overestimation of pure pixels.

The above-mentioned fuzzy methods often have poor performance in dealing with spectral variability and mixed pixels. Current fuzzy clustering and classification methods focus on the clustering characteristics of land cover types, ignore the clustering characteristics of mixed pixels, and apply a single point (a single or interval-valued point) to represent the centers of land cover types. However, intraclass variability cannot be represented by a single signature [24]. First, from the perspective of spectral diversity, the clusters of land cover types should be regions in spectral space due to the spectral diversity of remote sensing data. Taking a body of water as an example, the internal areas of water may be different in depth and composition,

resulting in different spectra at these locations. These areas are entirely bodies of water, so these locations are expected to belong to the core of bodies of water. Second, the membership degree of each pixel is calculated by the distance between it and these centers in current clustering-based methods. From the perspective of spectral mixing, this means that other pixels are mixed by these center points in different proportions, which is unreasonable; for example, a pixel in the core of a water body should not be mixed with the centers of water and centers of other land cover types. In reality, the spectral characteristics of mixed pixels should be a mixture of those of any pixel in clusters of land cover types. For example, a mixed pixel along a water body may be a mixture of grasslands and deep waters or a mixture of grasslands and shallow waters. Therefore, determining enough pure pixels for land cover types and establishing mixing relationships between these pure pixels and mixed pixels are the two keys for establishing MFs. Currently, many algorithms have been developed for estimating endmembers or endmember bundles as pure pixels [25], which is itself a very difficult and ill-posed problem [9], [24], [26]; alternatively, spectral indices are adopted to capture the full variability in vegetation spectra [10], i.e., pixels with an NDVI>0.7 are selected as pure pixels of vegetation. This method requires the selection of a strict threshold to ensure that the selected pixels are pure. Therefore, some pure pixels may be lost, for example, a pixel with an NDVI = 0.69. Another unavoidable fact is that there are many spectral indices for some land cover types, such as water and vegetation, and the performance of these indices varies greatly. In addition, it is difficult for us to establish spectral indices for some land cover types. In other words, it is difficult to apply suitable spectral indices and corresponding thresholds to capture the full variability of each land cover type. For the second key issue, many methods are available for estimating the proportions of different endmembers in a mixed pixel. However, most of these methods use a limited number of endmembers or endmember bundles [10], [26] for this task. Fuzzy unmixing methods [27] estimate the membership degrees or abundance fractions by calculating the closeness between synthetically mixed spectra *with all possible endmember combinations* and the observed pixel spectra; however, their computational complexity does not scale well with the number of endmembers [26]. In other words, these faults result in limited classification performance in wetland mapping. In summary, the intrinsic fuzziness of wetlands, spectral variability, and mixed-pixel problems together make it very difficult to generate MFs for land cover types in wetlands, which remains a challenge in wetland classification and mapping.

This study introduced a novel MF generation method that comprehensively considers the intrinsic fuzziness of wetlands, spectral variability, and mixed pixels. To capture the full spectral variability of the land cover types, the cores of the land cover types in spectral space were detected by combining the clustering characteristics and spectral indices. As mentioned earlier, it is difficult to draw a clear boundary line between fuzzy wetland components, but we can determine some areas as transition zones between these fuzzy wetland components. Therefore, *transition zones were used as an auxiliary land cover type in*

this study. Second, the remote sensing images were divided into small granules in spectral space, and a training set was used to classify these granules into four types: pure labeled granules, impure labeled granules, SGs, and UGs. Labeled and IGs were used to determine the core components; that is, pure labeled granules completely belonged to a land cover type, while IGs were between two land cover types. Third, the clustering characteristics combined with spectral indices were combined to detect the core components for each land cover type via a self-learning process; that is, some constraints with spectral indices were designed for the land cover types. Then, all the granules in the core components and satisfying spectral index constraints were treated as PGs, and the other granules were treated as BGs. Thus, pixels in PGs of C land cover types were regarded as pure pixels of C land cover types, and other pixels were boundary pixels between these C types. Fourth, considering that the spectra of mixed pixels may be a combination of the spectra of pure pixels of different land cover types and that the number of pure pixels is very large, the membership degrees of these boundary pixels were calculated by the sparse reconstruction method [28], [29]. Therefore, the proposed method was named the $C+1$ FMG method in this study, and the contributions of this study included the following.

1) Mixed pixels were treated as an auxiliary type for generating MFs.
2) Full spectral variability was expressed by combining clustering and spectral characteristics.
3) A method for calculating the membership degrees of boundary pixels based on core components was derived.
4) The $C+1$ FMG was found to have better performance than the MFs generated from the existing MF generation methods.

The rest of this article is organized as follows. In Section II, the main idea for the $C+1$ FMG is described. In Sections III and IV, the Beidagang wetland natural reserve was used as an example to test the performance of the proposed method. Section V is the discussion. Finally, Section VI concludes this article.

II. METHODOLOGY

First, existing clustering-based fuzzy classification methods only consider the clustering characteristics of land cover types but ignore the clustering characteristics of mixed pixels; Fig. 1(a) illustrates this problem. In this figure, two types of pixels were assumed: water and vegetation. Due to the atmospheric effects, illumination and topographic changes, and intrinsic variations in the spectral signatures of materials [9], the spectral signatures of all pixels of each type are variable, and these two types of pixels exhibit two clusters with different shapes in spectral space. Because of the large number of mixed pixels, these mixed pixels may also exhibit clustering characteristics.

Second, in the existing clustering-based fuzzy classification methods, one spectrum is used to represent the center of a land cover type, and the membership degree of an unknown type pixel is determined by the distance between the pixel and two centers. Obviously, the spectral variability was ignored. For example, in Fig. 1(a), pixels 1, 2, and 3 were assumed to be
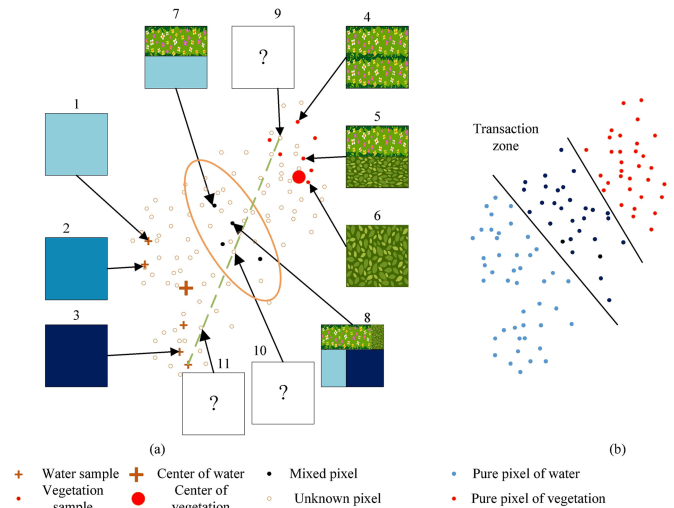

Fig. 1. Illustration of the spectral variability and spectral mixing between water and vegetation. It was assumed that pixels 1, 2, and 3 were pure pixels of water, and pixels 4, 5, and 6 were pure pixels of vegetation. Pixels 7 and 8 were mixed pixels, and pixels 9, 10, and 11 were unknown type pixels.

water samples and represented shallow, moderate, and deep water, respectively, while pixels 4, 5, and 6 were assumed to be vegetation samples and represented reeds, grassland, and the transition zone between them, respectively. The center could be calculated for these samples, the variation between pure samples was ignored, and the membership value of the mixed pixels could not be correctly calculated. For example, mixed pixel 7 was a mixture of shallow water and grassland; thus, the membership degree of pixel 7 should be determined by pure pixels 1 and 4. Similarly, mixed pixel 8 was a combination of deep water, shallow water, reeds, and grassland; thus, its membership degree should be calculated by pure pixels 1, 3, 4, and 6.

Third, a mixed pixel could be a mixture of any pure pixels of different types. For example, the unknown type pixel 10 may be a mix of pure pixels of water and vegetation that were not selected as training samples, such as pixel 9. Furthermore, a mixed pixel may be in the core of a land cover type when spectral diversity must be considered. In Fig. 1, a mixed pixel can be at any location on the green dotted line [27]; thus, the unknown type pixel 11 may be a mixed pixel. This means that it is not sufficient to select pure pixels only by using clustering characteristics, as this approach may lead to the overestimation of pure pixels.

To consider the above three issues when constructing fuzzy MFs, we built MFs for C land cover types; then, C types of pure pixels were selected as training samples. In addition to these C types of training samples, some samples in the transition zones were selected as training samples for the auxiliary type in this study. It is well known that pixel-level classification methods require considerable computational and memory resources. We segmented an image into small granules by the weighted FCM, and each granule contained several pixels with high spectral similarity. These granules were considered the basic processing units in this study and were classified into four types—purely labeled, impurely labeled, and SG and UGs—based on the number and types of training pixels in these granules. The $C+1$
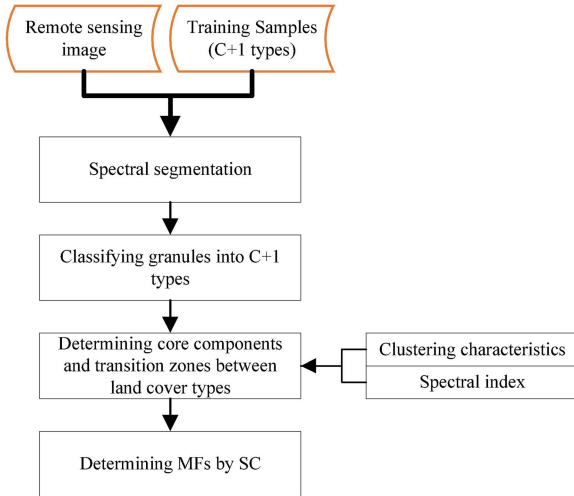
Fig. 2. Diagram of the proposed method.

Fig. 3. Hierarchical cluster tree [20].

Fig. 4. Illustration of the four types of granules in spectral space.

types of PGs (PGs of the *C* target class and one type of complete BG) and impure labeled granules were used to determine the core components of the land cover types and the transition zones between different types, and some spectral index constraints were integrated to purify these PGs. Finally, the membership values of the BGs were determined via the sparse reconstruction method. A diagram of the proposed method is shown in Fig. 2.

A. Spectral Segmentation of Remote Sensing Images

It is well known that classification at the pixel level is time consuming. Alternatively, clustering-based methods are useful for reducing the running time of classification [10], [30] and expressing spectral diversity [31], which segment a remote sensing image into small clusters or granules in spectral space. These granules can then be used as units for classification and other image analysis tasks. In this study, the hierarchical clustering process based on the FCM algorithm with the weighted Euclidean distance was adopted, and the full dataset X was clustered into T leaves by the FCM algorithm. The weighted Euclidean distance was determined as follows:

$$d_{ik} = \sum_{j=1}^{M} \frac{(x_{ij} - v_{kj})^2}{\sigma_j^2} \qquad (1)$$

where d_{ik} is the weighted Euclidean distance between sample x_i and center v_k and σ_j is the standard deviation of dimension j of the dataset. The number of samples N_G in a node was used as the termination criterion in this study. If a node does not reach the termination condition, it is split repeatedly; otherwise, it cannot be split and is treated as a leaf. The hierarchical tree is shown in Fig. 3, and the dotted and solid circles represent the intermediate and leaf nodes, respectively. In this study, all the leaves were named granules.

For the parameters of the weighted FCM algorithm, the number of children at a node had little effect on the classification accuracy, while the maximum number of iterations and the termination error had large effects; thus, the values of these two parameters were selected according to the literature.
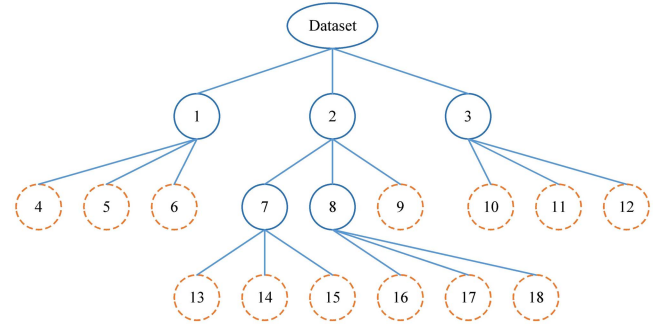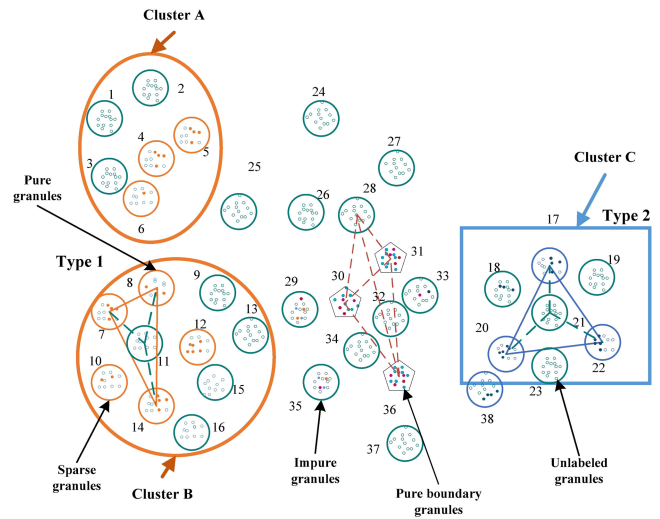
B. Classification of Granules Into Four Types

As discussed in Section I, there are large mixed pixels in middle-resolution remote sensing data, especially when the study area is complex, such as a wetland environment. It is difficult to select enough high-quality samples for target land cover types via supervised fuzzy classification methods. Therefore, in this study, a limited number of pure and mixed pixels were selected as a training dataset; i.e., the training dataset included *C* land cover types, and mixed pixels were treated as an auxiliary type and were used to mask these granules. Then, we found that some granules contain no training pixels, while others contain some labeled pixels. Therefore, a granule can be expressed as $G = \{\text{lp}_i\} \cup \{\text{up}_j\}$, where $\{\text{lp}_i\}(0 \leq i \leq N_{\text{lp}})$ and $\{\text{up}_j\}(0 \leq j \leq N_{\text{up}})$ refer to the labeled and unlabeled pixels in each granule, respectively. Fig. 4 illustrates the distribution of labeled and UGs; land cover type 1 contained clusters A and B with different shapes; type 2 contained cluster C; granules 4, 5, 6, 7, 8, 10, 12, 14, 17, 20, 22, 29, 30, 31, 33, and 38 were labeled; and the others were unlabeled. For granules with labeled pixels, some granules may contain only one type of labeled pixel; however, due to spectral uncertainties, some labeled granules may contain several types of labeled pixels. Obviously, a granule with many labeled pixels of a single type was most likely to be

inside a land cover type, and a granule with multiple types of labeled pixels must be in the transition zone between different types.

To distinguish the PGs from the others, the number and type of labeled pixels in a granule were used to classify the granules into four types:

1) *UGs,* which contained no labeled pixels, i.e., $N_{lp} = 0$;
2) *PGs,* which had only one type of labeled pixel and were larger than a certain threshold;
3) *SGs,* which contained only one type of labeled pixel, but the number of labeled pixels was greater than 0 and less than the threshold;
4) *IGs,* which had more than one type of labeled pixel.

It is clear that Gs $=$ UGs $\cup$ PGs $\cup$ SGs $\cup$ IGs. In this study, the threshold for distinguishing between SG and PG was determined by the inflection point method. First, we counted the number of labeled pixels in granules that had only one type of labeled pixel, calculated the frequency of these numbers and constructed a line graph. The threshold was subsequently determined by the inflection point of this graph. In Fig. 4, PGs 4, 5, 7, 8, and 14 are PGs of type 1; granules 17, 20, and 22 are PGs of type 2; granules 30, 31, and 36 are PGs of the transition zone; granules 29, 33, and 35 are IGs; granules 6, 10, 12, and 18 are SGs; and the others are UGs.

It was assumed that PGs and IGs were at the core of land cover types and in the transition zones between types, respectively, meaning that the PGs certainly belonged to a land cover type and could be treated as *CGs* and that a CG of a land cover type contained pixels in the cores of geographical objects of the same type. The *BGs* were located between clusters of different land cover types, so a BG contained pixels in the fuzzy boundaries of geographical objects.

Notably, Fig. 4 illustrates the distribution of the four types of granules in spectral space. Obviously, all PGs cannot reflect the distributions of the two types or the transition zone between them. Therefore, as detailed in the Section II.C, a self-learning process was designed to detect other PGs of two land cover types and transition zones. The centers of these granules can be used to represent them because of the high similarity of pixels in each granule.

C. Determination of the Core and Boundary Components of Land Cover Types With Clustering Characteristics and Spectral Indices

Fig. 4 illustrates that the spectral diversity or variability of each land cover type cannot be described by these initial PGs. In contrast, if all PGs of each land cover type could be detected, the spectral diversity could be fully expressed by these PGs. As discussed above, it was not sufficient to detect all PGs by using only clustering characteristics. In this section, the clustering characteristics and spectral indices of the land cover types were combined to determine all PGs. To capture the full spectral variability, the initial PGs were used as seeds, topological analysis of the granules in spectral space was introduced to generate candidate PGs, and the spectral characteristics were subsequently incorporated into this process to restrict these candidates.

First, all centers of PGs and IGs were used for this task and managed by the cover tree [34] to improve the efficiency of the neighbor query. The definitions of the CG and fringe granules were first introduced by the notion of the *k*-nearest neighborhood.

Definition 1 (IGC): If all the *k*-nearest neighbors of a *PG* are also *PGs* and have the same land cover type, then this PG represents an IGC.

Definition 2 (FGC): If a PG and its *k*-nearest neighbors have different land cover types, or its *k*-nearest neighbors contain an IG, then it is an FGC.

The UGs and IGs could be determined by checking whether they were CGs according to Definition 3.

Definition 3 (NPG): For a UG or SG, if its *k* nearest neighbors are IGCs with the same land cover type and satisfy the corresponding spectral index constraints, then it is an NPG of the corresponding land cover type.

For example, in Fig. 4, where $k = 3$, granule 20 was a PG, and its neighbors were PGs (granules 18, 21, and 38 are PGs); thus, according to Definition 1, granule 20 was an IGC. However, the neighbors of granule 38 were granules 18, 20, and 36; granules 18 and 20 were PGs of type 2; and granule 36 was a PG of the boundary; thus, according to Definition 2, granule 38 was an FGC. Granule 21 was a UG, and all of its neighbors (granules 17, 20, and 22) were IGCs; thus, it was an NPG of type 2 according to Definition 3.

Notably, the concepts of the core and boundary of a land cover type in a given place are different from those of a cluster. For example, in Fig. 4, granule 6 was a BG of cluster *A*, but it was a CG of type 1. On the other hand, if spectral index constraints are not considered in Definition 3, the PGs of some land cover types may be overestimated due to the multidimensionality of remote sensing data. The spectral characteristics were incorporated into Definition 3 to restrict these candidates in this study. Due to the complexity and vagueness of the wetland environment, it was difficult to define strict spectral index constraints for each land cover type, and threshold selection was also difficult. Alternatively, relatively loose constraints were adopted in this study. For example, the NDVI of vegetation had to be less than 0.3, the MNDWI [35] of vegetation could not be larger than 0, and the threshold for these constraints could not necessarily be too strict.

Currently, three strategies can be used to find the optimal *k* for Definition 1, Definition 2, and Definition 3: First, to find the optimal *k* for all testing samples, manually adjusting the *k* value is a common method. Lall and Sharma [36] suggested that the fixed optimal *k*-value should be $k = \sqrt{n}$ (where $n > 100$ is the number of training samples); second, the optimal *k* for each class [37], [38] can be found using the following equation:

$$k_{c_m} = \min\left(\alpha + \left[\frac{k * N(c_m)}{\max\{N(c_j)|j = 1, 2, \ldots, C\}}\right]\right), m$$
$$= 1, 2, \ldots, C \qquad (2)$$

where $N(c_m)$ denotes the size of class c_m in the training set, $\max\{N(c_j)\}$ is the size of the largest class, α is a nonnegative integer used for maintaining a reasonable minimum value of

k_{c_m}, C is the number of classes, and k is the original input integer for defining the nearest neighbors. Third, the optimal k value was found for each testing sample [39] or each training sample [29], [40] based on the reconstruction framework or other methods. The literature has shown that the reconstruction framework has better accuracy than the other two methods in most cases, but this method is too complex and time consuming. When the dataset is highly sparse and has uncertain attributes, the classification accuracy is worse than that of FKNN classification [41]. The k-influence space (IS_k) method [42] can be used to automatically find the optimal k value for each sample; another advantage of this method is that it needs no parameters, which saves the trouble of parameter tuning. Zhu et al. [43] redefined the space based on NNs and RNNs. The concept of an NN can be simply described as follows. Let x_i and x_j be two samples of a dataset. If x_i is a neighbor of x_j and x_j is a neighbor of x_i at the same time, then x_i and x_j are NNs of each other [44]. The NNs of each sample can be found by the NN search algorithm, and the NaNE is equal to the search round r in which the algorithm reaches a stable searching state; the NN of sample x_i is expressed as $\mathrm{NN}(x_i)$, while the number of $\mathrm{NN}(x_i)$s is expressed as $\mathrm{NaN}(x_i)$. The maximum neighborhood graph is constructed by connecting each point x_i to its $\mathrm{Max}(\mathrm{NaN}(x_i))$ nearest neighbors. For detailed information about the NN, we refer the reader to [43] and [44]. The RNNs of object x_i are the points that have x_i as one of their k-nearest neighbors, expressed as $\mathrm{RNN}(x_i)$. Then, the k-influence space of x_i was expressed as follows:

$$\mathrm{IS}_k(x_i) = \mathrm{NN}_k(x_i) \cup \mathrm{RNN}_k(x_i) \tag{3}$$

where k is determined by the NN search algorithm; that is, $k = \mathrm{Max}(\mathrm{NaN}(x_i))$. The IS_k neighbors may be different for each sample in the graph, which is suitable for automatically finding optimal neighbors for samples with complex data structures. In addition, this method does not need to set or tune any parameters during application.

An iterative process is designed to detect enough PGs. First, all centers of UGs, PGs, SGs, and IGs are calculated, as shown in Fig. 4, while the centers of PGs and IGs are used as seeds to construct a cover tree. Then, the IGC and FGG sets can be found for each type in terms of Definition 1 and Definition 2, and the NPGs in UGs and SGs can be found according to Definition 3. All the found centers of these NPGs are added to the cover tree, and the IGC and FGC sets are also updated. This process is repeated until the number of PGs is unchanged; that is, all the CGs of each land cover type are detected. During this process, the number of $C{+}1$ PGs may increase, and the presence of BGs limits the increase in the number of target granules, while the number of granules increases. Finally, all the pure pixels of the target classes and boundary pixels are detected, as shown in Fig. 1(b). Finally, the BGs can be expressed as follows:

$$\mathrm{BGs} = Gs - \bigcup_c \mathrm{PGs}' = \mathrm{UGs}' \cup \mathrm{PGs}^M \cup \mathrm{SGs}' \cup \mathrm{IGs}' \tag{4}$$

where PGs' are the final pure granules of C target land cover classes, PGs^M is the final pure granule of the auxiliary land cover

---

Algorithm 1: Determine the PG and BG.

   Input: UGs, SGs, SGs, IGs
   Output: final PGs, BGs
   Repeat:
   Find the optimal k with one of the three strategies.
   Determine IGC and FGC by Definition 1 and
     Definition 2;
   Determine the candidate NPG by Definition 3;
   Purification of candidate NPGs by spectral index
     constraints
   Until the number of PGs is unchanged
   Set the final PGs;
   The BGs are set by (4).

---

type, and UGs', SGs', and IGs' are the remaining unlabeled, sparse, and impure granules, respectively.

Fig. 1(b) illustrates the results of this process. Although the clusters of the two types have different shapes, all the internal granules of the two types could be detected, and the transition zones between the two types could be clearly described. Therefore, the spectral diversity of land cover types could be fully expressed. The performance of the three strategies for determining neighborhoods was investigated in the experiment. The specific algorithm flow is described in Algorithm 1.

D. Determination of the MFs and Remote Sensing Image Classification

In the Section II.C, PGs of C land cover types and BGs of these types were detected. The pixels in PGs' are treated as pure pixels, and the membership degrees are set to 1; the membership degrees of other types are set to 0. The other pixels in PGs^M, UGs', SGs', and IGs' are the boundary pixels.

In this section, the sparse reconstruction method [28], [29] based on LPPs [45] is adopted to calculate the membership degree of pixels in these mixed pixels. The centers of the PGs are $X \in R^{d \times n} = [x_1, \ldots, x_n]$, and the centers of the BGs are $Y \in R^{d \times n} = [y_1, \ldots, y_m]$, where n, m, and d represent the numbers of PGs, BGs, and bands, respectively. These PGs are used to reconstruct each BG with the goal that the distance between $X w_i$ (where $w_i \in R^n$ denotes the reconstruction coefficient matrix) and y_j is as small as possible. For the linear sparse mixing model, each BG can be decomposed into a linear combination of PGs as follows:

$$y_j = WX + \varepsilon \tag{5}$$

where $W \in R^n$ is the reconstruction coefficient or the correlation between the center of PGs and the center of a BG and ε is the noise value. To generate a sparse reconstruction coefficient for y_j, the objective function of the sparse reconstruction method [27], [28] is expressed as follows:

$$\min_W \|XW - X\|_F^2 + \rho_1 \|W\|_1 + \rho_2 \mathrm{Tr}\left(W^T XLX^T W\right), \ W \geq 0 \tag{6}$$

where $\|W\|_1$ is an ℓ_1-norm regularization term and $W \geq 0$ means that each element of W is nonnegative. $L = D - S$ is

the Laplacian matrix that measures the relational information between bands, and S refers to the similarity matrix between bands calculated by the radial basis function $f(a, b) = \exp(-\frac{\|a-b\|_2^2}{2\sigma^2})$ (where σ denotes the kernel width). D is a diagonal matrix, i.e., the ith diagonal element in D, where $D_{ii} = \sum_{k=1}^{d} S_{ik}$. ρ_1 and ρ_2 are two tuning parameters. The larger the value of ρ_1 is, the sparser the W; ρ_2 is used to control the order of magnitude of the LPPs [28]. The optimization algorithm of (6) is introduced in [28] and [29]. After optimizing (6), the weight matrix W can be obtained, which indicates the correlations between PGs and BGs y_j. Specifically, a positive weight (i.e., $w_{i,j} > 0$) indicates that the ith PG and y_j are positively correlated, while a negative weight (i.e., $w_{i,j} < 0$) means that their correlation is negative. In particular, a zero weight (i.e., $w_{i,j} = 0$) means that there is no correlation between them.

The sparse reconstruction algorithm is time consuming, i.e., at least $O(n^2 * d)$ for predicting each BG, where n is the number of PGs. Sometimes the number of detected PGs may be large; thus, it is necessary to speed up this algorithm. However, the spectra of each BG could be a combination of those of any PG; thus, it is necessary to select PGs that are strongly related to a BG by similarity measures. We tested the performance of several similarity measures, such as the Euclidean distance, the weighted Euclidean distance, the SAM, the SID, the SAM-SID mixed measure, and the JM-SAM [47], [48], which is a combination of the deterministic spectral angle mapper and the stochastic Jeffries–Matusita measure by the tangent [47]. That is, the JM-SAM is used to calculate the distances between y_j and PGs of each land cover type and sort these distances; then, K top strongly related PGs from PGs′ for each land cover type can be selected and used to reconstruct y_j by (6), where X contains $K*C$ centers of PGs and $K*C$ is much smaller than the total number of PGs. The weight matrix W is calculated by optimizing (6). The JM-SAM was selected for this study because it has a higher classification accuracy than other measures.

The membership degree of BG y_j belonging to land cover type c can be calculated by

$$\mu_{jc} = \frac{\sum_{t=1, \text{PG}_t \epsilon \text{PG}'_c}^{K*C} w_{jt}}{\sum_{t=1}^{K*C} w_{jt}}, (w_{jt} > 0) \qquad (7)$$

where PG'_c is the pure granule of land cover type c and PG_t is the tth pure granule.

Like in other fuzzy clustering methods, the principle of the maximum membership degree is used to determine the types of unlabeled samples, which can be expressed as $u_{ih} > \max_{\substack{h \neq j \\ j = 1, 2, \ldots, C}} u_{ij}$. Although salt-and-pepper noise could be observed in the results, some small fuzzy objects could be detected. That is, nonsmoothed results are beneficial for the extraction of small objects, such as drains, puddles, and dirt roads.

E. Computational Complexity Analysis

The computational complexity of the proposed method is the sum of two contributions. The complexity of step 1 is

Fig. 5.   (a) *Suaeda salsa* and (b) withered plants.

analyzed in [30] as $L \times O(CNd)$, where C is the number of clusters, N is the number of pixels, d is the number of attributes, and L is the maximum number of levels estimated by $L = \text{Int}(\log_C N / N_G + 1)$. The complexity of step 2 is $O(N_{Gs})$, where N_{Gs} is the number of granules. For step 3, each iteration needs to construct a cover tree, and the computational complexity of constructing the cover tree is $O(\delta^6 N_{\text{PG}} \ln N_{\text{PG}})$ [27], where N_{PG} is the number of centers for constructing the cover trees and δ is a bounded expansion constant. Suppose that T iterations are needed; then, the computational complexity of this step should be $T \times O(\delta^6 N_{\text{PG}} \ln N_{\text{PG}})$. For step 4, the computational complexity is $O((KC)^2 N_{\text{BG}} d)$, where $K * C$ is the number of PGs used to reconstruct a BG and N_{BG} is the number of boundary granules. Because the number of granules is far less than the number of pixels, the computational complexity of steps 2, 3, and 4 should be less than that of step 1. Therefore, the computational complexity of the proposed method should be $L \times O(CNd)$, and the running time analysis in the experiment will reflect this.

III. STUDY AREA AND DATASET

The Beidagang wetland is south of Tianjin Municipality and covers approximately 230 km^2; this wetland is an important station on the East Asian–Australian Flyway, one of the nine important migratory routes in the world [49]. This region contains two zones: the Beidagang wetland natural reserve and the Beidagang reservoir. This study focused on natural reserves, which include river wetlands, constructed wetlands, and swamp wetlands. Its main land cover types include grassland, lakes, rivers, narrow ditches, marshes, and bare soil. The main plant types include *Phragmites communis*, *Scripus planiculmis*, *Typha angustifolia*, and *Suaeda salsa* [49]. As a halophyte, *Suaeda salsa* plays an active role in soil restoration after being planted in saline soil and can increase soil nutrient content and improve soil fertility. After the autumn rainy season, the water content in the soil decreases, while the salt content in the soil increases. When the soil salt content reaches 1%–1.6%, the plant stems and leaves turn red, which can distinguish *Suaeda salsa* from other green vegetation, as shown in Fig. 5(a). In addition, this reserve contains a large area of withered aquatic and terrestrial vegetation. These withered plants strongly affect the water quality of the wetland, as shown in Fig. 5(b).

In this study, two cloud-free multispectral high-resolution images from the Sentinel-2 satellite were used. The data were acquired on 30 September 2020 and 21 September 2021, and the

TABLE I
NUMBERS OF TRAINING AND TEST SAMPLES

| Type	2020		2021	
	Number of training samples	Number of test samples	Number of training samples	Number of test samples
Water	29 020	243 194	36 774	307 510
Bare soil and impervious surfaces	3006	35 439	4941	22 542
Green lands	2226	156 792	5809	100 379
Suaeda salsa	1284	16 642	1474	39 170
Withered plants	1504	17 696		
Transition zone	5103	--	3605	--
Total	42 143	469 763	52 603	469 601
Cover percentage	4.83%	53.80%	6.03%	53.85%
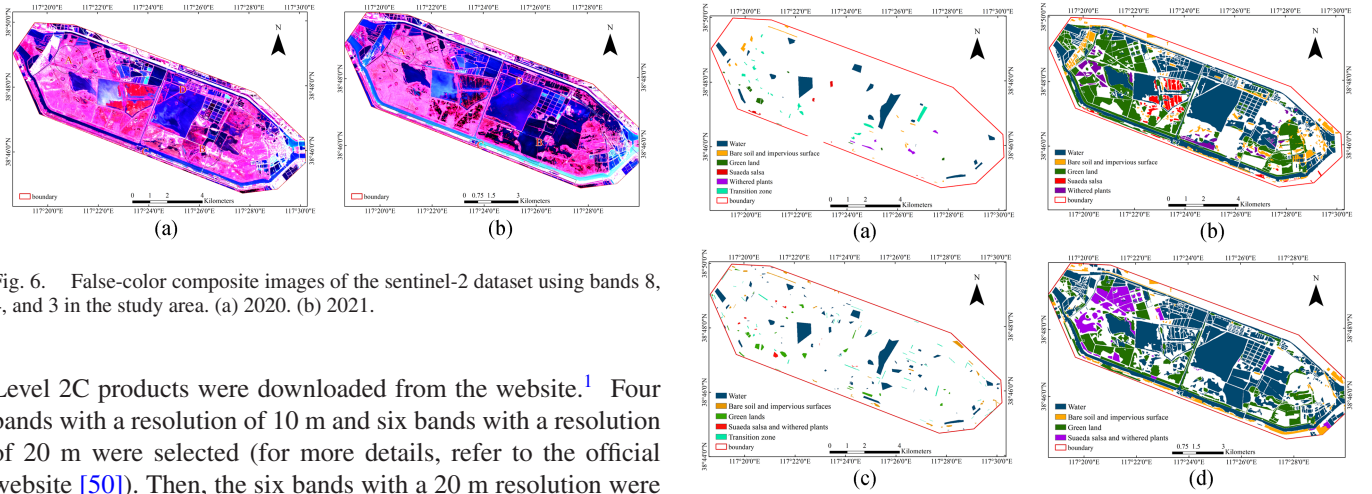
Fig. 6. False-color composite images of the sentinel-2 dataset using bands 8, 4, and 3 in the study area. (a) 2020. (b) 2021.

Level 2C products were downloaded from the website.[1] Four bands with a resolution of 10 m and six bands with a resolution of 20 m were selected (for more details, refer to the official website [50]). Then, the six bands with a 20 m resolution were super-resolved to 10 m by DSen2 [51], while these selected bands were masked by a crisp boundary. The natural color composite image with bands 4, 3, and 2 is shown in Fig. 6. In 2020, we observed a large area of *Suaeda salsa*; therefore, the reserve was classified into five types: water, green land, bare soil, and impervious surface, *Suaeda salsa* and withered plants. Region A in Fig. 6(a) was mainly covered with green vegetation and withered plants, as well as many small water bodies, such as small ditches and puddles. Regions B and D were mainly marshlands and artificial fishponds. Region C was the riverbank and was mainly composed of green vegetation, bare land, and *Suaeda salsa*. In 2021, the area of the water body increased significantly, and many areas where *Suaeda salsa* grew in 2020 were submerged, as shown in Fig. 6(b). This made it difficult for us to discover contiguous areas of *Suaeda salsa* in the study area. Therefore, in this year, *Suaeda salsa* and withered plants were combined into one land cover type.

The training and test samples were collected by visual interpretation using Worldview-2 images from the same period. As discussed before, the Sentinel-2 images have many mixed pixels; thus, in addition to selecting pure pixels for the target land cover types, this study also selected some transition zones as an auxiliary type. The training and testing samples in 2020 are shown in Fig. 7(a) and (b), respectively. The numbers of training

Fig. 7. Training and test samples of the two datasets. (a) Training samples in 2021. (b) Testing samples in 2021. (c) Training samples in 2021. (d) Testing samples in 2021.

and test samples are listed in Table I. The training and testing samples from 2021 are shown in Fig. 7(c) and (d), respectively, and cover approximately 6.03% and 53.85% of the study area.

IV. RESULTS AND DISCUSSION

In this section, the results of the proposed method were reported to verify its performance and were compared with those of the CFDT [52], the SIIT2-FCM [53], the SS-AIT2FCM algorithm [54], and adaptive FKNN classification, which finds the optimal k value for each class [37], [38], from the perspective of classification accuracy, i.e., overall accuracy (OA) and kappa coefficient. Due to the imbalance of target types in the study area, the macro $F1$-score was adopted to measure the classification accuracy. In addition to these methods, the fractional SU method [24], which has been proven to have good performance [9], was also compared.
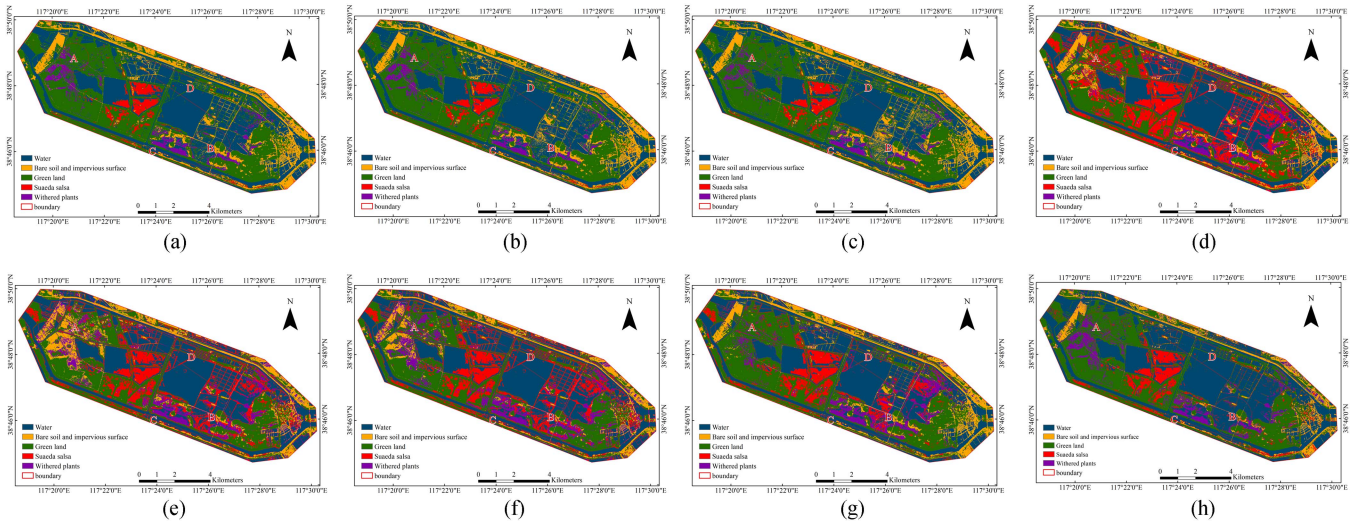
[1][Online]. Available: https://scihub.copernicus.eu/dhus

Fig. 8. Classification results in 2020. (a) Fixed optimal $k = 40$. (b) Optimal k for each class. (c) IS. (d) FKNN. (e) SIIT2-FCM. (f) SS-AIT2FCM. (g) CFDT. (h) Fractional SU.

The number of samples in a node was used as the threshold in this study and initialized to 150. For the parameters of weighted FCM during hierarchical tree building, the number of children in a node was set to 3, the maximum number of iterations was 100, and the termination error was 0.001.

For the first image, 12 917 granules were obtained. The training dataset was used to classify these granules into four types, and the numbers of UGs, PGs, IGs, and SGs were 8187, 1969, 147, and 2614, respectively. Among the PGs, water, bare soil, green lands, *Suaeda salsa,* and withered plants represented 1076, 219, 178, 72, and 365, respectively. For the second image, 10 956 granules were obtained, and the numbers of UGs, PGs, IGs, and SGs were 6135, 2188, 296, and 2337, respectively.

A. Classification Results

To detect the core part of each type, a KNN with a fixed option k value, a KNN with the optimal k for each class, and the k-influence space (IS_k) method were investigated in this step individually. The spectral index constraints used in Definition 3 for identifying candidates in this study included the following.
1) Water: IF MNDWI <0, THEN RETURN FALSE.
2) Bare soil: IF NDVI>0.3 OR MNDWI>0 THEN RETURN FALSE.
3) Green land: IF NDVI<0.3 OR Band (red) $>$ Band (green) OR MNDWI>0 THEN RETURN FALSE.
4) *Suaeda salsa*: IF NDVI<0.3 OR Band (red) $<$ Band (green) OR MNDWI>0 THEN RETURN FALSE.

Notably, the green and red bands in the Sentinel-2 image are shown in green and red, respectively. *Suaeda salsa* is a type of vegetation, and its distribution is very similar to that of green land. The significant difference in its spectrum is that when *Suaeda salsa* leaves turn red, the reflectivity in the green band is lower than that in the red band; at this time, the reflectance of green vegetation in the green band is greater than that in the red band. Notably, there was no obvious regularity in the spectrum

of the withered plants, and currently, there is no spectral index for this type; thus, in this study, we did not define spectral index constraints for this type.

The fixed optimal k value was selected manually; that is, the band number (N_b) of the image was set as the step size, and the other parameters were fixed. We let $k_f = t \times N_b (2 \leq t \leq 10)$ and increase t from 2 to 10 to determine the inner part; then, the membership degrees of the pixels in the transition zones were determined by using the sparse reconstruction algorithm. In this experiment, the OA was highest when t was equal to 4. To find the optimal k for each class, we let $\alpha = 2 \times N_b$ and the original k equal k_{f_b}; then, the optimal k_{c_m} could be calculated for each class with (2). The process of calculating the IS_k neighbors of each center requires no parameters. The parameters ρ_1 and ρ_2 in step 4 can be set to 10 according to the suggestions in [27] and [28], and the sparse reconstruction algorithm had the same weights for sparseness and the order of magnitude of the LPP part.

For 2020, the classification results of the proposed method are shown in Fig. 8(a)–(c). Small water bodies in region A could be detected by all three strategies. Region B contained some swamps, and in addition to water bodies, there were many submerged plants and emergent plants. Three strategies misclassified some of the patches as bare soils, and the misclassification of the third one was the most serious. In region C, the three strategies could distinguish red *Suaeda salsa* from green vegetation and bare soil. In region D, ridges between fishponds could be identified, and the vegetation types were classified as green lands or bare soil, which is similar to what was observed in our field investigation. The OA, kappa coefficient, and macro $F1$ measure of the proposed method are listed in Table II. The OAs of the first two strategies were 93.10%, while their macro $F1$ measures were 0.8736 and 0.8717; thus, the first two strategies exhibited similar performances. The third strategy was less accurate than the first two. The three strategies had similar computational complexities, while the computational

|		C+1 FMG			FKNN	SIIT2-FCM	SS-AIT2FCM	CFDT	Fractional SU
		Fixed optimal k	Optimal k for each class	IS					
2020	OA (%)	**93.10**	93.10	92.60	82.01	82.53	83.39	87.78	87.65
	Kappa	**0.8877**	0.8878	0.8802	0.7245	0.729	0.7412	0.8059	0.8
	Macro F1	**0.8736**	0.8717	0.8669	0.6659	0.6326	0.6427	0.7402	0.7595
	Running time (s)	244+196	244+194	244+246	633	403	1260	**4**	244+68
2021	OA (%)	94.06	**94.06**	94.04	92.6	87.97	87.34	90.87	89.12
	Kappa	0.8844	**0.8844**	0.8842	0.858	0.771	0.7588	0.8237	0.7998
	Macro F1	0.8914	**0.8915**	0.8911	0.8524	0.7714	0.7524	0.7763	0.7949
	Running time (s)	307+176	307+196	307+240	712	160	884	**4**	307+68

The best results are highlighted in bold.
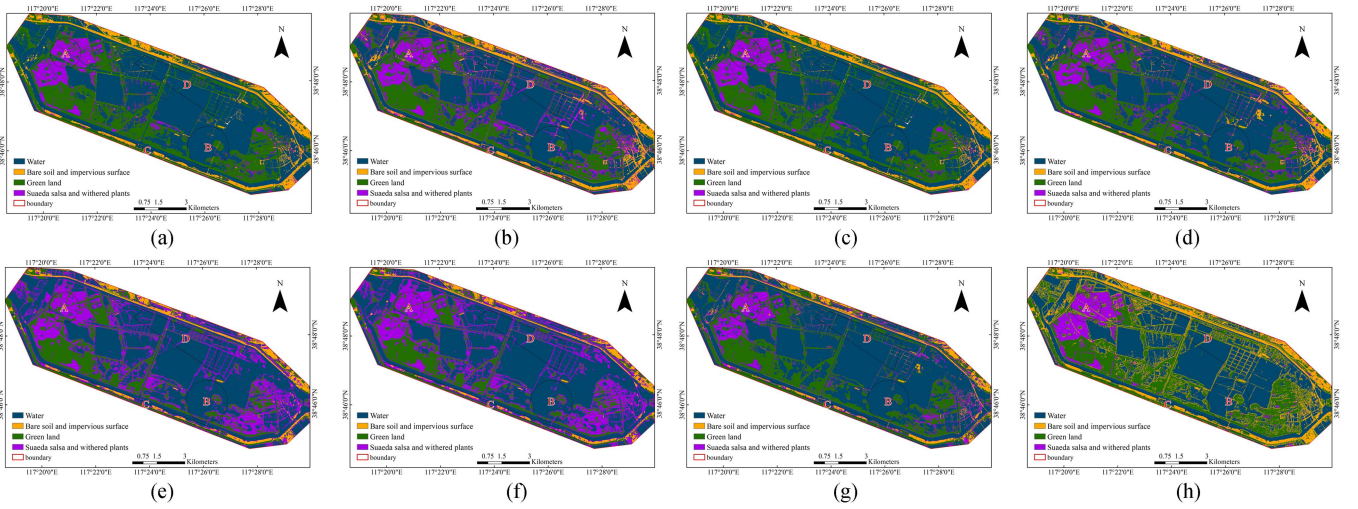
Fig. 9. Classification results in 2021. (a) Fixed optimal $k = 40$. (b) Optimal k for each class. (c) IS. (d) FKNN. (e) SIIT2-FCM. (f) SS-AIT2FCM. (g) CFDT. (h) Fractional SU.

complexity of the third strategy was slightly greater than that of the first two strategies.

The classification results of the proposed method in 2021 are shown in Fig. 9(a)–(c). Small water bodies in region A could be detected by the proposed method. The water area in region B increased significantly. In region C, the area of red *Suaeda salsa* decreased significantly. In region D, ridges between fishponds could also be identified. The three strategies had similar accuracies, as high as 94%.

B. Comparison With Other Methods

To evaluate the performance of the proposed method, the FKNN, SIIT2-FCM, SS-AIT2FCM, and CFDT methods were compared, and the training samples of five target land cover types were used. For FKNN, the optimal k for each class was found by (1), while the original k value was set to $\sqrt[2]{N}$ (N is the number of training pixels) and $\alpha = \sqrt[2]{N}/4$. For SIIT2-FCM, the two fuzzifier values were set to 2 and 5. For SS-AIT2FCM, the fuzzifier value and the adaptive factors for each type were

calculated automatically according to the authors' suggestions. For the CFDT, the number of children for each node was set to 3, the node size was set to 5, and the other parameters were the same as those in the proposed method in step 1.

For the fractional SU, the automated endmember extraction method [55] adopted in [24] cannot be used to distinguish endmembers of different land cover types with high spectral similarity, which has been described previously [55]. Therefore, the local density peak clustering method [56] was adopted to extract endmember bundles in this study. We first calculated the local density of each granule by NNs, and two representative transfer rules [56] were used to find local density peaks and clusters. Then, PGs were used to label these local clusters. If a local cluster contained one type of PG, its corresponding local density peak was an endmember of this type. In this way, 41, 8, 8, 3, and 3 endmembers of five land cover types were extracted from the first image, and 60, 9, 13, and 2 endmembers of four types were extracted from the second image.

For 2020, the results for the FKNN, SIIT2-FCM, SS-AIT2FCM, CFDT, and fractional SU datasets are shown in

Fig. 8(d)–(h). Many land cover types were misclassified as red *Suaeda salsa* by the FKNN, SIIT2-FCM, and SS-AIT2FCM methods. For example, in regions A and C, this land cover type was obviously overestimated. Moreover, these three methods misclassified withered plants as bare soil in region A. These three methods had poor ability to detect small objects. For example, a few small water bodies could be detected in region A. The CFDT and fractional SU had similarly high performances as did the FKNN, SIIT2-FCM, and SS-AIT2FCM; however, the CFDT misclassified withered plants as green vegetation or *Suaeda salsa* in region A, and in region B, it seriously misclassified water as *Suaeda salsa*. The fractional SUs had poor classification accuracy for bare soil, and some roads and ridges between fishponds were not clear. The OA, kappa coefficient, macro $F1$ measure, and running time of these methods are listed in Table II. The classification accuracy of the $C+1$ FMG was significantly greater than that of the FKNN, SIIT2-FCM, SS-AIT2FCM, CFDT, and fractional SU methods, especially for the macro $F1$ measure. SIIT2-FCM and SS-AIT2FCM use a single curve to represent the spectrum of a land cover type, implying that these two methods cannot express the spectral diversity of land cover types and leading to the macro $F1$ measures of these two methods being far less common than those of other methods. The CFDT could take spectral diversity into account to a certain extent (different training samples of a land cover type can exist on different leaves in the CFDT), and the overall accuracies of the CFDT and the fractional SU were greater than those of the FKNN, SIIT2-FCM, and SS-AIT2FCM but were still obviously less than those of the proposed method.

For 2021, the OA of FKNN was the highest among the compared methods, but FKNN exhibited poor performance in detecting small water bodies. SIIT2-FCM and SS-AIT2FCM had the lowest classification accuracy, and the areas of the land cover types *Suaeda salsa* and withered plants were seriously overestimated. The results of the fractional SU seriously overestimate the area of bare soil. Therefore, the proposed method can fully consider spectral diversity and mixed pixels, and its classification performance is significantly better than that of the other methods.

V. DISCUSSION

To analyze the performance of the proposed method, several aspects are discussed in this section. To simplify the discussion, only the first image was discussed.

A. Analyzing the Effect of the Auxiliary Type

As discussed before, there were many mixed pixels in the boundary between land cover types, and this study treated the mixed pixels as an auxiliary type. To analyze the roles of this auxiliary type in this section, the boundary samples were removed, which means that the training samples only contained samples of five target types. The settings of the parameters were consistent with the settings in the first section. The OA, kappa coefficient, and macro $F1$ measure of the classification results of the first image are listed in Table III. The OA, kappa coefficient, and macro $F1$ measure of these results were lower than those in

TABLE III
CLASSIFICATION ACCURACY OF THE PROPOSED METHOD WITH TRAINING SAMPLES OF FIVE TARGET TYPES

	Fixed optimal k	Optimal k for each class	IS
OA (%)	89.20	**90.59**	90.27
Kappa	0.8270	**0.8472**	0.8404
Macro F1	0.7489	**0.7795**	0.7500

The best result is highlighted in bold.

TABLE IV
CLASSIFICATION ACCURACY OF THE PROPOSED METHOD WITH THE DISTANCE METRIC

	Fixed optimal k	Optimal k for each class	IS
OA (%)	90.29	**90.32**	89.99
Kappa	0.8431	**0.8437**	0.8387
Macro F1	0.7811	**0.7812**	0.7779

The best result is highlighted in bold.

Section IV-A but still larger than that of the other methods. This means that using boundary simples as an auxiliary type can help determine CG and BGs and improve the classification accuracy.

B. Analyzing the Effect of Sparse Reconstruction

In this study, we assumed that the spectrum of a mixed pixel is composed of the spectra of pure pixels of the target types. To verify this hypothesis, the Euclidean distance was used to replace the sparse reconstruction in step 4. First, the centers of all the CGs of the five target types detected in step 3 were used to construct a cover tree and find the k nearest neighbors of each unknown type of pixel. We suppose that these neighbors had H types and that the membership degrees of the pixels in these types of granules were determined by

$$u_{ij} = \frac{1}{\sum_{k=1}^{H} \left(d'_{ij}/d'_{ik} \right)^{2/(m-1)}} \tag{8}$$

where u_{ij} is the membership degree of sample i belonging to class j, d'_{ij} is the shortest distance from sample i to type j, and d'_{ik} $(1 \leq k \leq H)$ is the shortest distance from sample i to the H types.

The settings of the other parameters were consistent with the settings in the first section. The OA, kappa coefficient, and macro $F1$ measure of the classification results are listed in Table IV. The OA, kappa coefficient, and macro $F1$ measure of the three strategies were very similar and lower than those in Section IV-A but also larger than those of the other methods. This showed that the membership degrees of some BGs cannot be determined by their nearest PGs. Moreover, the sparse reconstruction algorithm can be used to effectively find some PGs for IGs, and the spectra of these IGs were mixed with the spectra of these PGs; thus, using these PGs to determine the membership degree of this BG should be more reasonable than using its nearest PGs.

TABLE V
CLASSIFICATION ACCURACY OF THE PROPOSED METHOD WITH NO SPECTRAL INDEX CONSTRAINTS OR STRICT SPECTRAL INDEX CONSTRAINTS

	No spectral index constraints			Strict spectral index constraints		
	Fixed optimal k	Optimal k for each class	IS	Fixed optimal k	Optimal k for each class	IS
OA (%)	92.59	91.45	91.18	90.14	91.8	90.81
Kappa	0.8793	0.8613	0.8569	0.8398	0.867	0.8515
Macro F1	0.8663	0.8337	0.8355	0.7976	0.8467	0.8171

C. Analyzing the Influence of Spectral Index Constraints

As discussed before, spectral index constraints were used to eliminate mixed pixels from clusters of land cover types. Therefore, in this section, we focused on the effects of spectral index constraints under three strategies. First, the constraints were removed, and the other parameters were the same as those in Section IV-A. Second, the loose constraints were replaced by a group of strict constraints according to the literature. For example, the NDVI threshold for green land is greater than 0.7. These constraints were as follows.

1) Water: IF MNDWI >0 THEN RETURN TRUE.
2) Bare soil: IF NDVI>−0.2 && NDVI<0.4 AND MNDWI<0 THEN RETURN TRUE.
3) Green land: IF NDVI>0.7 AND Band (red) < Band (green) AND MNDWI<0 THEN RETURN TRUE.
4) *Suaeda salsa*: IF NDVI>0.5 AND Band (red) > Band (green) AND MNDWI<0 THEN RETURN TRUE.

By comparing Tables I and V, we can see that when the spectral constraints were removed, the classification accuracies under the three strategies decreased because of the spectral index constraints, as listed in Section IV-A, were beneficial for determining the PGs and improving the performance of the proposed method. However, when these loose constraints were replaced by strict constraints, the performance of the proposed method decreased and was even worse than that of no spectral index constraints. These constraints were too strict to filter out some PGs; that is, some PGs were mistakenly regarded as BGs, and the spectral diversity could not be fully expressed by these generated PGs. As a result, in step 4, some BGs could be reconstructed from the appropriate PGs. Therefore, the relatively loose spectral constraints adopted in this study are beneficial for expressing spectral diversity and improving the performance of the proposed method.

D. Effect of Parameters in the Sparse Reconstruction

The parameters in four steps could affect the performance of the proposed method. Zhang et al. [29] recommended that the node number in the weighted FCM has a modest effect on performance, while an increase in the granule size threshold reduces the accuracy of classification. In step 2, the threshold for determining PGs also affected the accuracy, and the empirical value was adopted in this study [31], [32]. In step 3, the optional k in strategies 1 and 2 affects the performance of the proposed method, and this optional k should be selected manually, as

mentioned in Section IV-A. For strategy 3, no parameter should be selected. Therefore, in this section, we focused only on the influence of parameters in the sparse reconstruction process.

We analyzed the influences of parameters ρ_1 and ρ_2 in step 4. Let $\rho_1, \rho_2 \in \{0.1, 1, 5, 10, 20, 50\}$ and the parameters in steps 1–3 be the same as those in Section IV-A. Then, the combinations of ρ_1 and ρ_2 were used to test the classification performance, and the results are listed in Table VI. The values of ρ_1 and ρ_2 can significantly affect the classification performance. The best performance was obtained using the combination of 1 and 20, and the corresponding OA, kappa, and macro $F1$ measures were 93.30%, 0.8910, and 0.8787, respectively. The worst performance was obtained with the combination of 50 and 0.1, and the corresponding OA, kappa, and macro $F1$ measures were 92.28%, 0.8749, and 0.8532, respectively. The element values on the diagonals in Table VI are marked in bold, and the element values below the diagonal were less than the values above the diagonal. Since parameters ρ_1 and ρ_2 were used to control the sparsity and the order of magnitude of the LPP, the increase in the sparsity of the selected PGs reduced the classification accuracy, which means that using more PGs to reconstruct the unknown granules improved the classification performance. This illustrated the assumption that a mixed pixel could be a mixture of any pure pixel of different types.

Because the intrinsic fuzziness, spectral variability, and mixed pixels were considered at the same time in middle-resolution multispectral image classification, the solution should be sophisticated. First, in middle-resolution remote sensing images, the proportions of mixed pixels are relatively high, and these mixed pixels form the clusters of different sizes and shapes. These clusters can be detected by the local density peak clustering method [55]. This means that the clustering characteristic of mixed pixels cannot be ignored, which was proven in Section V-A, and using mixed pixels as an auxiliary type can substantially improve the classification accuracy. Second, the shapes of clusters cannot be ignored when spectral variability is considered. In the existing studies, a single center or endmember cannot express spectral variability, which was also proven in Section IV-B. The classification accuracy of the proposed method was substantially greater than that of these single-center methods and the fractional SU. However, expressing the full spectral variability is still an open problem in the existing studies. In this study, we used the cores of clusters to express the full spectral variability and used the relatively loose spectral index constraints to eliminate mixed pixels in

TABLE VI
CLASSIFICATION ACCURACY OF THE PROPOSED METHOD WITH DIFFERENT COMBINATIONS OF ρ_1 AND ρ_2

ρ_1 \ ρ_2		0.1	1	5	10	20	50
0.1	OA (%)	**93.00**	93.11	93.21	93.30	93.26	93.19
	Kappa	**0.8859**	0.8879	0.8894	0.8908	0.8903	0.8892
	Macro F1	**0.8695**	0.8736	0.8765	0.8784	0.8777	0.8757
1	OA (%)	92.67	**92.99**	93.20	93.27	*93.30*	93.18
	Kappa	0.8809	**0.8859**	0.8893	0.8904	*0.8910*	0.8891
	Macro F1	0.8607	**0.8695**	0.8753	0.8775	*0.8787*	0.8757
5	OA (%)	92.56	92.87	**93.03**	93.19	93.24	93.23
	Kappa	0.8792	0.8840	**0.8866**	0.8892	0.8899	0.8899
	Macro F1	0.8586	0.8664	**0.8720**	0.8754	0.8770	0.8776
10	OA (%)	92.65	92.80	92.99	**93.10**	93.16	93.16
	Kappa	0.8806	0.8830	0.8860	**0.8877**	0.8888	0.8888
	Macro F1	0.8604	0.8642	0.8704	**0.8736**	0.8757	0.8761
20	OA (%)	92.70	92.80	92.98	93.03	**93.05**	93.00
	Kappa	0.8813	0.8829	0.8858	0.8867	**0.8870**	0.8864
	Macro F1	0.8609	0.8636	0.8694	0.8718	**0.8736**	0.8733
50	OA (%)	92.28	92.38	92.59	92.67	92.68	**92.73**
	Kappa	0.8749	0.8766	0.8800	0.8812	0.8815	**0.8823**
	Macro F1	0.8532	0.8570	0.8628	0.8655	0.8661	**0.8675**

The best results are highlighted in bold.

cores; Sections IV-B and V-C proved the effectiveness of this method. Third, to achieve the membership values of mixed pixels or boundary pixels, we used the sparse reconstruction method to replace the shortest distance or highest similarity between boundary pixels and cores. In Section V-B, this approach effectively improved the classification results, and Section V-D illustrated the effects of two parameters of the sparse reconstruction method. This section also proved that it is necessary to consider these factors comprehensively. To our knowledge, existing methods only consider some of these factors, so our method showed substantial improvement in classification accuracy compared with the existing fuzzy classification methods.

Importantly, in this study, no smoothing operation was adopted (in fact, using the Gaussian convolution function in our experiment can improve the overall accuracy by approximately 0.5%), and nonsmoothed results were beneficial for the extraction of small objects, such as drains, puddles, and dirt roads. On the other hand, because spatial correlation and heterogeneity coexist in geographic areas, four types of mixed pixels exist in remote sensing images [57]. In complex wetland ecosystems, the four types of mixed pixels widely exist at the same time; thus, spatial correlation and heterogeneity should be fully considered, while addressing these four types of mixed pixels is beyond the scope of this study and will be discussed in the future.

Although the performance of the proposed method was better than those of the other methods, several limitations still exist. The first is that the proposed method seems complex. We simplify the complexity of the operations of the proposed

method in several ways. For example, we used the inflection point method to automatically select the threshold to distinguish between sparse granules and PGs in the granule classification step. In the CG and BG determination step, we provided three strategies for this task: the first two strategies were easy to implement, and the third strategy seemed complex; however, users did not need to manually set the parameters in this strategy. Therefore, readers can choose their preferred strategy in this step. The second disadvantage was that readers should manually set spectral index constraints because these constraints vary across different applications. The values of parameters ρ_1 and ρ_2 should also be set manually; to our knowledge, there is no automated way to determine these two parameters.

VI. CONCLUSION

Spectral diversity and mixed pixels are two important aspects that affect the performance of remote sensing classification and mapping. This study proposed a comprehensive method at the pixel level to generate MFs that simultaneously address spectral diversity and mixed pixels. First, the mixed pixels were treated as an auxiliary type due to the large number of mixed pixels in middle-resolution remote sensing images. Second, the clustering and spectral characteristics of the land cover types were integrated to obtain pure and mixed pixels of land cover types, and these pure and mixed pixels constructed the core and boundary components of the land cover types, respectively. This approach ensured the comprehensiveness and reliability of the

expression of spectral diversity. Because mixed pixels could be a mixture of any pure pixels of different types, the sparse reconstruction method was used to determine their membership degrees. The experiments showed that the proposed method can improve the classification accuracy compared with the existing MF generation methods.

Due to the complexity of wetland systems, it is difficult to map some small landscape units, such as ditches and puddles, at the pixel level from Sentinel-2 images by using existing MF generation methods. The experiment showed that the proposed method performed better at expressing small wetland components than the other methods. However, the ability to express small landscape units is scale dependent, and the MF downscaling method [58] could improve this ability; the small components could then be expressed at the subpixel level with this method.

REFERENCES

[1] T. Sun, W. Lin, G. Chen, P. Guo, and Y. Zeng, "Wetland ecosystem health assessment through integrating remote sensing and inventory data with an assessment model for the Hangzhou Bay, China," *Sci. Total Environ.*, vol. 566/567, pp. 627–640, Oct. 2016.

[2] P. P. Ryan, J. H. Geoffrey, and C. Gang, "How wetland type and area differ through scale: A GEOBIA case study in Alberta's boreal plains," *Remote Sens. Environ.*, vol. 117, pp. 135–145, Feb. 2012.

[3] K. S. Schmidt and A. K. Skidmore, "Spectral discrimination of vegetation types in a coastal wetland," *Remote Sens. Environ.*, vol. 85, no. 1, pp. 92–108, Apr. 2003.

[4] B. Somers and G. P. Asner, "Multi-temporal hyperspectral mixture analysis and feature selection for invasive species mapping in rainforests," *Remote Sens. Environ.*, vol. 136, pp. 14–27, Sep. 2013.

[5] I. Dronova, "Object-based image analysis in wetland research: A review," *Remote Sens.*, vol. 7, no. 5, pp. 6380–6413, May 2015, doi: 10.3390/rs70506380.

[6] S. Kaliraj, N. Chandrasekar, K. K. Ramachandran, Y. Srinivas, and S. Saravanan, "Coastal landuse and land cover change and transformations of Kanyakumari coast, India using remote sensing and GIS," *Egyptian J. Remote Sens. Space Sci.*, vol. 20, no. 2, pp. 169–185, Dec. 2017.

[7] C. Arnot and P. Fisher, *Mapping the Ecotone With Fuzzy Sets. Geographic Uncertainty in Environmental Security*. Berlin, Germany: Springer, 2007, pp. 19–32.

[8] P. F. Fisher, "Remote sensing of land cover classes as type 2 fuzzy sets," *Remote Sens. Environ.*, vol. 114, no. 2, pp. 309–321, Feb. 2010.

[9] R. A. Borsoi et al., "Spectral variability in hyperspectral data unmixing: A comprehensive review," *IEEE Geosci. Remote Sens. Mag.*, vol. 9, no. 4, pp. 223–270, Dec. 2021, doi: 10.1109/MGRS.2021.3071158.

[10] F. Xu, X. Cao, X. Chen, and B. Somers, "Mapping impervious surface fractions using automated fisher transformed unmixing," *Remote Sens. Environ.*, vol. 232, Oct. 2019, Art. no. 111311.

[11] V. Cross and A. Firat, "Fuzzy objects for geographical information systems," *Fuzzy Sets Syst.*, vol. 113, no. 1, pp. 19–36, Jul. 2000.

[12] J. C. Bezdek, R. Ehrlich, and W. Full, "FCM: The fuzzy C-means clustering algorithm," *Comput. Geosci.*, vol. 10, no. 2/3, pp. 191–203, 1984.

[13] J. M. Keller, M. R. Gray, and J. A. Givens, "A fuzzy k-nearest neighbor algorithm," *IEEE Trans. Syst., Man, Cybern.*, vol. SMC-15, no. 4, pp. 580–585, Jul./Aug. 1985.

[14] W. Pedrycz and J. Waletzky, "Fuzzy clustering with partial supervision," *IEEE Trans. Syst., Man, Cybern., B*, vol. 27, no. 5, pp. 787–795, Oct. 1997.

[15] D. T. C. Lai and J. M. Garibaldi, "A comparison of distance-based semi-supervised fuzzy C-means clustering algorithms," in *Proc. IEEE Int. Conf. Fuzzy Syst.*, 2011, pp. 1580–1586.

[16] C. Hwang and F. C. H. Rhee, "Uncertain fuzzy clustering: Interval type-2 fuzzy approach to C-means," *IEEE Trans. Fuzzy Syst.*, vol. 15, no. 1, pp. 107–120, Feb. 2007.

[17] I. Bloch, "Fuzzy sets for image processing and understanding," *Fuzzy Sets Syst.*, vol. 281, pp. 280–291, Dec. 2015.

[18] G. M. Foody and D. P. Cox, "Sub-pixel land cover composition estimation using a linear mixture model and fuzzy membership functions," *Int. J. Remote Sens.*, vol. 15, no. 3, pp. 619–631, 1994.

[19] X. Li, F. Ling, and Y. Du, "Super-resolution mapping based on the supervised fuzzy C-means approach," *Remote Sens. Lett.*, vol. 3, no. 6, pp. 501–510, 2012.

[20] X. Yang, Z. Xie, F. Ling, X. Li, Y. Zhang, and M. Zhong, "Spatio-temporal super-resolution land cover mapping based on fuzzy C-means clustering," *Remote Sens.*, vol. 10, no. 8, Aug. 2018, Art. no. 1212, doi: 10.3390/rs10081212.

[21] T. Cheng, M. Molenaar, and H. Lin, "Formalizing fuzzy objects from uncertain classification results," *Int. J. Geographical Inf. Sci.*, vol. 15, no. 1, pp. 27–42, 2001.

[22] F. Brubeck-Hernandez, T. Vladimirova, M. Pooley, R. Thompson, and B. Knight, "Zone management in precision agriculture using satellite imagery," in *Proc. NASA/ESA Conf. Adaptive Hardware Syst.*, 2019, pp. 65–71.

[23] V. Ilic and N. M. Ralevic, "Fuzzy squareness: A new approach for measuring a shape," *Inf. Sci.*, vol. 545, pp. 537–554, Feb. 2021.

[24] L. Drumetz, T. R. Meyer, J. Chanussot, A. L. Bertozzi, and C. Jutten, "Hyperspectral image unmixing with endmember bundles and group sparsity inducing mixed norms," *IEEE Trans. Image Process.*, vol. 28, no. 7, pp. 3435–3450, Jul. 2019, doi: 10.1109/TIP.2019.2897254.

[25] R. Liu and X. Zhu, "Endmember bundle extraction based on multiobjective optimization," *IEEE Trans. Geosci. Remote Sens.*, vol. 59, no. 10, pp. 8630–8645, Oct. 2021, doi: 10.1109/TGRS.2020.3037249.

[26] L. Ren, Z. Ma, F. Bovolo, and L. Bruzzone, "A nonconvex framework for sparse unmixing incorporating the group structure of the spectral library," *IEEE Trans. Geosci. Remote Sens.*, vol. 60, May 2022, Art. no. 5506719, doi: 10.1109/TGRS.2021.3081101.

[27] M. Petrou and P. G. Foschi, "Confidence in linear spectral unmixing of single pixels," *IEEE Trans. Geosci. Remote Sens.*, vol. 37, no. 1, pp. 624–626, Jan. 1999.

[28] S. Zhang, M. Zong, K. Sun, Y. Liu, and D. Cheng, "Efficient kNN algorithm based on graph sparse reconstruction," in *Proc. Int. Conf. Adv. Data Mining Appl.*, 2014, pp. 356–369.

[29] S. Zhang, X. Li, M. Zong, X. Zhu, and R. Wang, "Efficient kNN classification with different numbers of nearest neighbors," *IEEE Trans. Neural Netw. Learn. Syst.*, vol. 29, no. 5, pp. 1774–1785, May 2018, doi: 10.1109/TNNLS.2017.2673241.

[30] X. Jia and J. A. Richards, "Fast k-NN classification using the cluster-space approach," *IEEE Geosci. Remote Sens. Lett.*, vol. 2, no. 2, pp. 225–228, Apr. 2005.

[31] J. Guo and S. Du, "A multicenter soft supervised classification method for modeling spectral diversity in multispectral remote sensing data," *IEEE Trans. Geosci. Remote Sens.*, vol. 60, May 2022, Art. no. 5605517, doi: 10.1109/TGRS.2021.3079909.

[32] M. Ester, H. P. Kriegel, J. Sander, and X. Xu, "A density-based algorithm for discovering clusters in large spatial databases with noise," in *Proc. 2nd Int. Conf. Knowl. Discov. Data Mining*, 1996, pp. 226–231.

[33] G. Ulutagay and E. Nasibov, "Fuzzy and crisp clustering methods based on the neighborhood concept: A comprehensive review," *J. Intell. Fuzzy Syst.*, vol. 23, no. 6, pp. 271–281, 2012, doi: 10.3233/IFS-2012-0519.

[34] A. Beygelzimer, S. Kakade, and J. Langford, "Cover trees for nearest neighbor," in *Proc. 23rd Int. Conf. Mach. Learn.*, 2006, pp. 97–104.

[35] H. Xu, "Modification of normalised difference water index (NDWI) to enhance open water features in remotely sensed imagery," *Int. J. Remote Sens.*, vol. 27, no. 14, pp. 3025–3033, Feb. 2007.

[36] U. Lall and A. Sharma, "A nearest neighbor bootstrap for resampling hydrologic time series," *Water Resour. Res.*, vol. 32, no. 3, pp. 679–693, 1996.

[37] B. Li, Q. Lu, and S. Yu, "An adaptive k-nearest neighbor text categorization strategy," *ACM Trans. Asian Lang. Inf. Process.*, vol. 3, pp. 215–226, 2004.

[38] H. Patel and G. S. Thakur, "An improved fuzzy k-nearest neighbor algorithm for imbalanced data using adaptive approach," *IETE J. Res.*, vol. 65, no. 6, pp. 780–789, May 2018, doi: 10.1080/03772063.2018.1462109.

[39] S. Zhang, M. Zong, K. Sun, Y. Liu, and D. Cheng, "Efficient kNN algorithm based on graph sparse reconstruction," in *Advanced Data Mining and Applications*, vol. 8933, X. Luo, J. X. Yu, and Z. Li, Eds. Berlin, Germany: Springer, 2014, doi: 10.1007/978-3-319-14717-8_28.

[40] Z. Bian, C. M. Vong, P. K. Wong, and S. Wang, "Fuzzy KNN method with adaptive nearest neighbors," *IEEE Trans. Cybern.*, vol. 52, no. 6, pp. 5380–5393, Jun. 2022, doi: 10.1109/TCYB.2020.3031610.

[41] W. Jin, A. K. H. Tung, J. Han, and W. Wang, "Ranking outliers using symmetric neighborhood relationship," in *Advances in Knowledge Discovery and Data Mining*, vol. 3918, W. K. Ng, M. Kitsuregawa, J. Li, and K. Chang, Eds. Berlin, Germany: Springer, 2006, doi: 10.1007/11731139_68.

[42] A. Wahid and C. S. R. Annavarapu, "NaNOD: A natural neighbour-based outlier detection algorithm," *Neural Comput. Appl.*, vol. 33, no. 6, pp. 2107–2123, Jun. 2021, doi: 10.1007/s00521-020-05068-2.

[43] Q. Zhu, J. Feng, and J. Huang, "Natural neighbor: A self-adaptive neighborhood method without parameter K," *Pattern Recognit. Lett.*, vol. 80, pp. 30–36, 2016, doi: 10.1016/j.patrec.2016.05.007.

[44] J. C. Bezdek, *Pattern Recognition With Fuzzy Objective Function Algorithms*. New York, NY, USA: Plenum Press, 1981.

[45] X. Wu and S. Zhang, "Synthesizing high-frequency rules from different data sources," *IEEE Trans. Knowl. Data Eng.*, vol. 15, no. 2, pp. 353–367, Mar./Apr. 2003, doi: 10.1109/TKDE.2003.1185839.

[46] W. Zhang et al., "K-value adaptive KNN algorithm using annular filter," *Comput. Eng. Appl.*, vol. 55, no. 23, pp. 45–52, 2019.

[47] S. Padma and S. Sanjeevi, "Jeffries Matusita based mixed-measure for improved spectral matching in hyperspectral image analysis," *Int. J. Appl. Earth Observ. Geoinf.*, vol. 32, pp. 138–151, Oct. 2014, doi: 10.1016/j.jag.2014.04.001.

[48] S. Shanmugam and P. Srinivasa Perumal, "Spectral matching approaches in hyperspectral image processing," *Int. J. Remote Sens.*, vol. 35, no. 24, pp. 8217–8251, Dec. 2014, doi: 10.1080/01431161.2014.980922.

[49] X. Mo et al., *Vegetation and Plant Diversity of Beidagang Wetland*. Beijing, China: China Ocean Press, 2020.

[50] Sentinel-2 User Guide, 2021. [Online]. Available: https://sentinels.copernicus.eu/web/sentinel/user-guides/sentinel-2-msi

[51] C. Lanaras, J. Bioucas-Dias, S. Galliani, E. Baltsavias, and K. Schindler, "Super-resolution of sentinel-2 images: Learning a globally applicable deep neural network," *ISPRS J. Photogramm. Remote Sens.*, vol. 146, pp. 305–319, Dec. 2018, doi: 10.1016/j.isprsjprs.2018.09.018.

[52] W. Pedrycz and Z. A. Sosnowski, "C-fuzzy decision trees," *IEEE Trans. Syst., Man, Cybern., C*, vol. 35, no. 4, pp. 498–511, Nov. 2005.

[53] L. T. Ngo, D. S. Mai, and W. Pedrycz, "Semi-supervising interval type-2 fuzzy C-means clustering with spatial information for multi-spectral satellite image classification and change detection," *Comput. Geosci.*, vol. 83, pp. 1–16, Oct. 2015.

[54] J. Xu et al., "Remote sensing image classification based on semi-supervised adaptive interval type-2 fuzzy C-means algorithm," *Comput. Geosci.*, vol. 131, pp. 132–143, Oct. 2019.

[55] B. Somers, M. Zortea, A. Plaza, and G. P. Asner, "Automated extraction of image-based endmember bundles for improved spectral unmixing," *IEEE J. Sel. Topics Appl. Earth Observ. Remote Sens.*, vol. 5, no. 2, pp. 396–408, Apr. 2012.

[56] D. Cheng, J. Huang, S. Zhang, X. Zhang, and X. Luo, "A novel approximate spectral clustering algorithm with dense cores and density peaks," *IEEE Trans. Syst., Man, Cybern., Syst.*, vol. 52, no. 4, pp. 2348–2360, Apr. 2022, doi: 10.1109/TSMC.2021.3049490.

[57] P. Fisher, "The pixel: A snare and a delusion," *Int. J. Remote Sens.*, vol. 18, no. 3, pp. 679–685, 1997, doi: 10.1080/014311697219015.

[58] Y. Lin and J. Guo, "Fuzzy geospatial object-based membership function downscaling," *Remote Sens.*, vol. 15, no. 7, 2023, Art. no. 1911, doi: 10.3390/rs15071911.

Jifa Guo received the B.S. degree in surveying and mapping engineering and the M.S. degree in cartography and geographic information engineering from Henan Polytechnic University, Jiaozuo, China, in 2004 and 2007, respectively, and the Ph.D. degree in cartography and geographic information systems from the Institute of Remote Sensing Applications, Chinese Academy of Sciences, Beijing, China, in 2010.

He is currently a Professor with Tianjin Normal University, Tianjin, China. His research interests include uncertainties in geospatial data, high-order fuzzy geographic information modeling and spatial analysis, and fuzzy processing and analysis of remote sensing data.

Shihong Du received the B.S. and M.S. degrees in cartography and geographic information systems from Wuhan University, Wuhan, China, in 1998 and 2001, respectively, and the Ph.D. degree in cartography and geographic information system from the Institute of Remote Sensing Applications, Chinese Academy of Sciences, Beijing, China, in 2004.

He is currently a Professor with Peking University, Beijing, China. His research interests include image knowledge representation and reasoning, urban remote sensing, urban landscape modeling and analysis with urban big data, and semantic understanding of multimodal spatial data.